Energy Storage Materials 71 (2024) 103546

Contents lists available at ScienceDirect

Energy Storage Materials

journal homepage: www.elsevier.com/locate/ensm

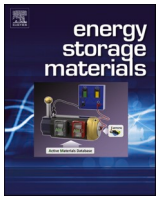

Promoting electrochemical rates by concurrent ionic-electronic conductivity enhancement in high mass loading cathode electrode

Ying Wang [a], Aleksandar S. Mijailovic [b], Tongtai Ji [a], Ercan Cakmak [c], Xianhui Zhao [c], Luyao Huang [a], Brian W. Sheldon [b,*], Hongli Zhu [a,*]

[a] Department of Mechanical and Industrial Engineering, Northeastern University, Boston, MA 02115, USA
[b] School of Engineering, Brown University, Providence, RI 02912, USA
[c] Manufacturing Science Division, Oak Ridge National Laboratory, Oak Ridge, TN 37831, USA

ARTICLE INFO

Keywords:
Cellulose nanocrystals
Electrode additive
Lithium-ion battery
Ionic conductivity
Electronic conductivity
Kinetics

ABSTRACT

Enhancing the fast charging capacity of thick electrodes with high mass loading is imperative in expediting the widespread adoption of electric vehicles. Nonetheless, the insufficient charge transfer kinetics of thick electrodes hinder the movement of effective electrons and ions, hence diminishing capacity at high current rates. Herein, we applied sustainable and biodegradable cellulose nanocrystals (CNCs) as electrode additives. It is the first time to simultaneously improve the electronic conductivity by optimizing the carbon dispersion and establishing electron transfer networks, as well as boosting the ionic conductivity of electrodes by shortening the ion transfer pathway. Specifically, the $LiNi_{0.6}Mn_{0.2}Co_{0.2}O_2$ electrodes incorporating 1% dual functional CNCs additive exhibit improved effective electrical conductivity from 0.11 to 0.16 S/m and risen effective ionic conductivity from 0.36 to 0.62 S/m, in comparison to counterpart electrodes without CNCs. Therefore, the 1% CNC electrode with a high mass loading of 27.0 mg/cm^2 delivers a discharge capacity of 128 mAh/g at 1 C, which is superior to that of the CNC-free electrodes (95 mAh/g). In short, this study presents a novel environmentally friendly, economically viable, and dual-functional electrode additive that enhances both electronic and ionic conductivities with the aim of facilitating the widespread adoption of fast-charging high mass loading electrodes.

1. Introduction

In light of the current energy scarcity and the pressing need to address environmental issues, electric vehicles (EVs) are emerging as a promising alternative to conventional automobiles. With their high energy densities and fast-charging capabilities, lithium-ion batteries (LIBs) serve as a reliable power source for EVs, enabling an exceptional cruising range while minimizing charging time [1]. In conjunction with the advancement of active materials possessing high specific capacity [2–4], enhancing the areal mass loading of active materials through increasing electrode thickness is a straightforward and effective approach to elevating the energy density of LIBs [5,6]. However, the thick electrodes with high mass loading present a significant difficulty in terms of their limited capacity during fast charging because of inadequate charge transfer kinetics. Consequently, improving the electronic and ionic conductivities of high mass loading electrodes can facilitate the efficiency of charge transport and improve their fast-charging capacity.

Utilizing structurally special or inherently high-performance electronic conducting agents and binders is a facile approach to optimize the charge transfer kinetics. For instance, two-dimensional carbons can shorten the electron transfer distance by generating a planar continuous electronic transfer network; unique binders with both high electronic and ionic conductivity can directly enhance both electron and ion transport of electrodes [7–10]. However, these materials are too pricey to be commercialized. From the standpoint of being more compatible with industrialization, it is sensible to employ cost-efficient approaches to construct percolating electronic and ionic conductive networks to improve charge transfer kinetics and achieve outstanding fast-charging capacity of electrodes [11,12].

Decreasing the porosity of electrodes to boost the contact between carbon particles (the most commercialized electronic conductive agent for LIBs) and enhancing the uniformity of carbon particle dispersion between carbon particles and active materials are two main strategies to establish an interconnected electronic transfer network and elevate the electronic conductivity of electrodes. In industrial production, the

* Corresponding authors.
E-mail addresses: brian_sheldon@brown.edu (B.W. Sheldon), h.zhu@neu.edu (H. Zhu).

https://doi.org/10.1016/j.ensm.2024.103546
Received 17 April 2024; Received in revised form 29 May 2024; Accepted 9 June 2024
Available online 10 June 2024

electrode can be densified by calendering [13] and carbon dispersion can be facilely enhanced by surfactant introduction [14], materials preparation procedures optimization [15], mixing time elongation [16,17], etc. Different from the mechanism of electrical conductivity increase, the enhancement of ionic conductivity of the electrode is primarily contributed by shortening the ion transfer path, such as increasing porosity and reducing tortuosity of electrodes [18–21]. Due to the different or even contradictory improving strategies in industrial manufacturing electrodes (for instance, compressed electrodes to reduce their porosity can boost their electronic conductivity but negatively impair their ionic conductivity), the predominant focus of the current publications has been singularly around the promotion of either electronic conductivity or ionic conductivity of electrodes. Currently, improving kinetics by concurrently enhancing the electronic and ionic conductivity of thick electrodes is challenging yet rewarding.

This study pioneered the use of earth-abundant, cost-efficient, and environmentally friendly biomass-derived cellulose nanocrystals (CNCs) as a dual-functional additive to simultaneously enhance the electronic and ionic conductivity of thick LIBs cathode for fast-charging. Compared with conventional $LiNi_{0.6}Mn_{0.2}Co_{0.2}O_2$ (NMC 622) cathode without CNCs additive, scanning electron microscopy (SEM) and X-ray computed tomography (XCT) results reveal that optimized electrodes exhibit enhanced dispersion of carbon, improving the electronic conductivity of electrodes. Meanwhile, the ionic conductivity of electrodes shows a positive correlation with the amount of CNCs additive. Simulation results illustrate the faster kinetics produced by the optimized electrode with the addition of CNCs. Furthermore, the 1% CNC electrode, with a high mass loading of 27.0 mg/cm^2, significantly enhances the capacity to 128, 87, and 50 mAh/g at current rates of 1, 2, and 3 C, respectively. These values are considerably greater than those achieved with a 0% CNC electrode that delivers capacities of 95, 37, and 19 mAh/g at 1, 2, and 3 C, respectively. Consequently, incorporating CNCs additive in the existing electrode slurry is favorable from an environmental, cost, and operational perspective, which holds great promise for the industrial development of thick electrodes with outstanding fast charging capacity and for the advancement of reliable EVs that are dependable.

2. Results and discussion

CNCs additive assists high mass loading thick electrodes in achieving faster kinetics through optimizing the charge transfer path, therefore simultaneously improving electronic and ionic conductivities. Fig. 1a and 1b intuitively portray the electron and ion transfer paths in electrodes with CNCs additive, respectively. Although CNCs are electrically insulating, they enhance the electronic conductivity of electrodes by optimizing the carbon distribution. In particular, the (200) β crystalline plane of CNCs containing rich layers of –CH– methine groups exhibits substantially hydrophobic properties [22], which can be used to improve the dispersion of hydrophobic nanomaterials [23,24]. Thereby, the incorporation of CNCs aids the dispersion of carbon nanoparticles, establishing interconnected electron transfer networks within electrodes and evidently enhancing their electronic conductivity. Furthermore, despite the distance between two untreated cellulose chains being too narrow to restrict the accessibility for Li^+ transfer [25–27], the CNCs additive can still improve the ionic conductivity of electrodes due to Li^+ being able to travel along the CNCs via a combination of hopping and vehicle mechanisms [28,29]. The hydroxyl (–OH) groups and sulfonic ($–SO_3H$) groups on CNC are available to anchor the Li^+ by forming Li bonds [30,31], which enables the hopping of ions from a donor to the nearest acceptor. Moreover, the vehicle mechanism might occur by the solvent carrying ions through the polymer. The presence of the highly porous structure of CNCs boosts solvent absorption and storage [32–34], allowing Li^+ transfer through the vehicle mechanism. Consequently, large amounts of CNCs deposited on the NMC surface can construct a unique ion transfer bridge, accelerating the ion transfer and increasing

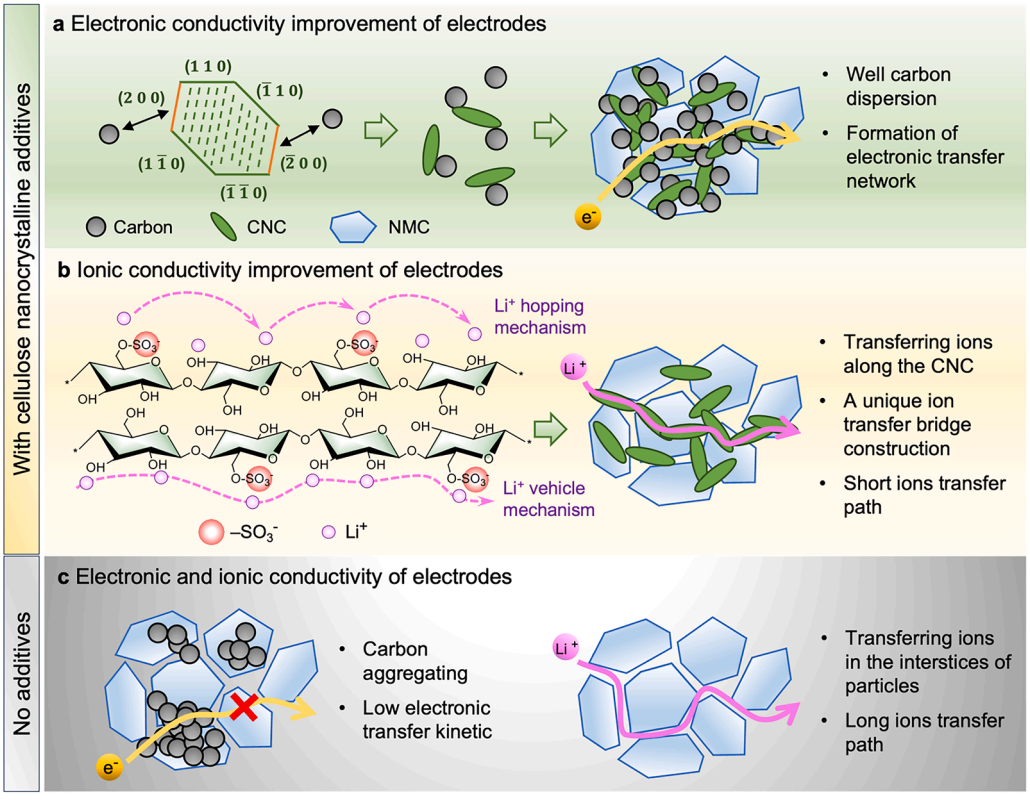

Fig. 1. Schematic of mechanisms of cellulose nanocrystalline additive in simultaneously improving (a) electronic and (b) ionic conductivity of the electrode, with (c) the electrode without additive as a reference.

the ionic conductivity of CNCs-added electrodes.

Fig. 1c illustrates the conventional electrode without CNCs additive, in which the charge transfer kinetics are insufficient to realize outstanding capacity at high charge rates. Specifically, the presence of non-uniformly distributed carbon results in the formation of carbon-free zones that hinder the construction of continuous electronic transmission networks. Thereby the electron transfer is hindered. Moreover, conventional electrodes lack an ion transfer bridge and the ions have to squeeze through the narrow and highly distorted spaces between particles. The comparable lengthy transfer path leads to sluggish ion transfer. Overall, the addition of an appropriate amount of CNCs is advantageous for enhancing both electron and ion transfer within electrodes and achieving enhanced kinetics. This facile strategy and affordable material can be extensively integrated into the existing commercial fast-chargeable thick electrodes and directly improve their capacity at high current rates.

CNCs are plentiful, cheap, and biodegradable cellulose nanomaterials derived from the bulk cellulose fibers originally from natural trees (Fig. 2a). The bulk cellulose composites of the regular cycle of ordered crystalline regions and amorphous regions. In accordance with the objectives of this work, the disordered amorphous components were removed using sulfuric acid hydrolyzing, leaving highly ordered cellulose crystalline regions. After sulfuric acid treatment, portions of –OH groups were converted to highly acidic –SO_3H groups on the CNCs [35]. The morphology of synthesized CNCs was characterized using atomic force microscopy, as portrayed in Fig. 2b. CNCs are rod-like structures with a high aspect ratio, measuring approximately 11 nm in width and 200 nm in length. This special structure aids CNCs in establishing interconnected bridges and networks on the NMC particle surface by randomly overlapping. In order to further confirm the chemical structure of CNCs, Fourier transform infrared spectroscopy (FTIR) and X-ray diffraction (XRD) were employed. The XRD results were collected and plotted in Fig. 2c. At 2θ values of 15 and 23°, the representative peaks of (110) and (200) corresponding to the cellulose I crystalline structure are observed, in which the (200) crystalline edge renders CNC with special hydrophobic properties. Additionally, the two minuscule peaks located at 2θ of 12 and 18 ° indicate the presence of a trace amount of cellulose II [36]. As shown in Fig. 2d, the representative spectrum of cellulose is observed by peaks at 3340, 1433, 1316, 1159, 1109, and 1058 cm^{-1}, which are associated with the O–H stretching vibration, C–H_2 symmetric bending, C–H_2 wagging vibration, C–C ring stretching, C–O symmetric stretching, and stretching vibration of C–O–C in pyranose ring, respectively [37,38]. The sample displays a characteristic peak at 2911 cm^{-1}, which corresponds to the C–H stretching vibration. This group imparts hydrophobic properties to the CNCs and assures carbon adsorption. In addition, the peak at 1204 cm^{-1} is caused by the stretching vibration of –S=O from –SO_3H [37].

To maximize the dispersion of CNCs in electrode slurries, a specific concentration of CNCs and polyvinylidene fluoride (PVDF) mixtures were initially prepared in N-methylpyrrolidone (NMP) solvent. Before blending CNCs with PVDF, as-hydrolyzed CNCs aqueous dispersion was freeze-dried to remove water while maintaining the highly porous structure of CNCs (**Fig. S1**). The CNCs cannot be dissolved into the organic solvent, and dispersion of CNC in NMP maintains its mesoporous structure after the solvent has gone away [32]. Although CNCs contain plentiful hydrophilic –OH groups that make undesirable dispersion in the organic solvent, the addition of a specific concentration of PVDF effectively prevents the rapid coalescence of CNCs in NMP (**Fig. S2**). Ideally, CNCs at a sufficiently low concentration enable acceptable dispersibility in NMP. However, this particular concentration is deemed

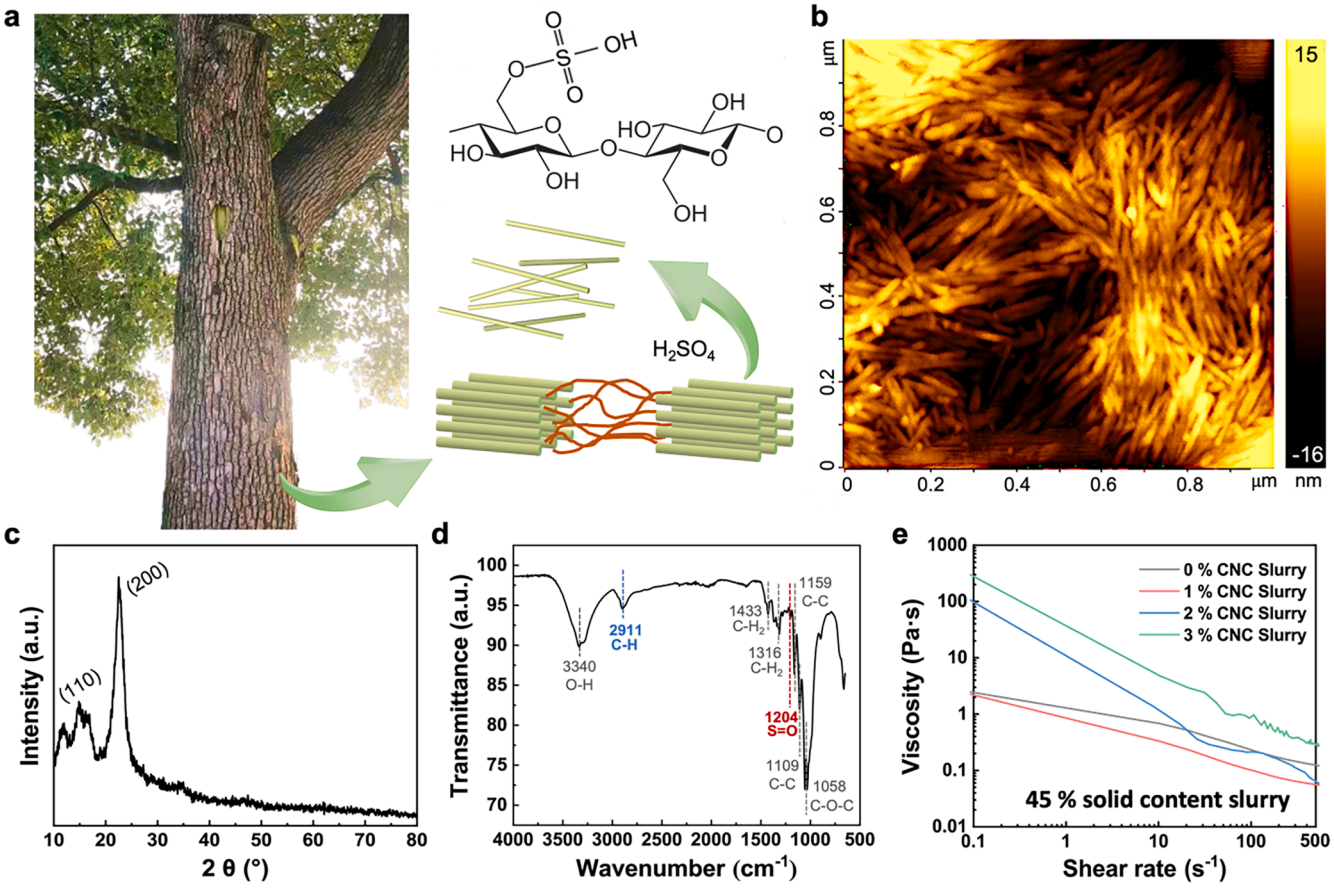

Fig. 2. CNCs and electrode slurries with CNCs additive. (a) Schematic illustration of the source and production process of obtained CNCs. (b) AFM image (c) XRD, and (d) FTIR of the synthesized CNCs. (e) The viscosity of electrode slurries composed of various amounts of CNCs.

unsuitable for the industrial production of electrode slurries. Industrialization requires electrode slurries with a high solid content to ensure cost-effectiveness and eco-friendliness. This is because the higher solid content results in reduced solvent consumption for slurry preparation and energy requirements during the drying process. Consequently, about 45% solid content electrode slurries were fabricated in this study, and a mixture consisting of 2.5% solid content PVDF and CNCs was prepared for mixing. **Fig. S3** presents digital images of electrode slurries containing varying amounts of CNCs during fabrication procedures. After mixing all components (labeled as add NMC), the 0 and 3% CNC electrode slurries exhibited thicker flow behavior than the other two slurries. Through prolonging 30 min of mixing, all slurries became macroscopically smooth and flowable.

In order to further reveal and understand the dispersion situation of components for electrode slurries with various amounts of CNCs, the rheological behavior of these slurries was evaluated. As portrayed in Fig. 2e, the viscosity of electrode slurries exhibited two distinct types of curves due to different mechanisms. For 0 and 1% CNC electrode slurries, their rheological behaviors are greatly impacted by the dispersion of carbon nanoparticles. Compared to 0% CNC electrode slurry, the slurry containing 1% CNCs exhibits a lower viscosity, indicating enhanced dispersion of carbon in the 1% CNC electrode slurry due to diminished interparticle shear forces. Unlike the previous two slurries, the 2 and 3% CNC electrode slurries present significantly elevated viscosity at low shear rates and an obvious inflection point around a shear rate of 60 s^{-1}, resulting from the heavy aggregation and network performance caused by the high concentration of CNCs [39]. The high viscosity of 3% CNC electrode slurry resulted from the inhomogeneous particle dispersion and corresponding high shear force between aggregated materials. These CNCs aggregations negatively affect the homogeneous dispersion of carbon particles and the formation of related electronic conductive networks.

After drying, the carbon dispersion of electrodes composed of various CNCs was characterized using SEM. Fig. 3a–d display the top view of 0, 1, 2, and 3% CNC electrodes. The 0% CNC electrode shows a negligible quantity of dark particles, which is further investigated in the following. The majority of the area is covered by gray NMC particles. With the inclusion of 1% CNCs, the dispersion of all particles was more uniform. With further increasing the CNCs content to 2 and 3%, large amounts of NMC are covered with dark powder. It is evident that the 1% CNCs additive maximizes the uniformity of particle distribution throughout the electrode.

To investigate the composition of the dark particles, elemental mapping of electrodes was applied. Fig. 3e shows a typical area with NMC particles wrapped by dark particles in the 1% CNC electrode where the carbon (C), oxygen (O), and fluorine (F) elements are labeled as fuchsia, green, and yellow, respectively. The elemental mapping results show that carbon nanoparticles rather than oxygen-contained CNC were responsible for the darkness of the particles, as the O signal barely overlapped the dark particles. The distribution of large amounts of carbon around NMC particles in 1% CNC electrode creates a network for electron transfer. Meanwhile, the F is observed throughout the electrode, elucidating the sufficient dispersion of PVDF. Identical results were confirmed in additional locations (**Fig. S4**). Carbon dispersion in the vertical direction has a significant impact on the electron transfer through thick electrodes, further affecting their rate performance. **Fig. S5** displays cross-sectional elemental mapping images of 0 and 1% CNC electrodes with C in fuchsia and O in green. In contrast to the 0 % CNC electrode, the 1% CNC electrode exhibits a more uniform carbon dispersion.

In order to conduct a more comprehensive analysis and identify the distributions of components in the electrode, XCT results were visualized in Fig. 4 via 3D reconstructions [40]. Compared to elemental mapping images that concentrate on local surface morphology, XCT is a powerful technique for scanning and marking various components in the whole electrode. To elucidate the impact of varying amounts of CNCs on

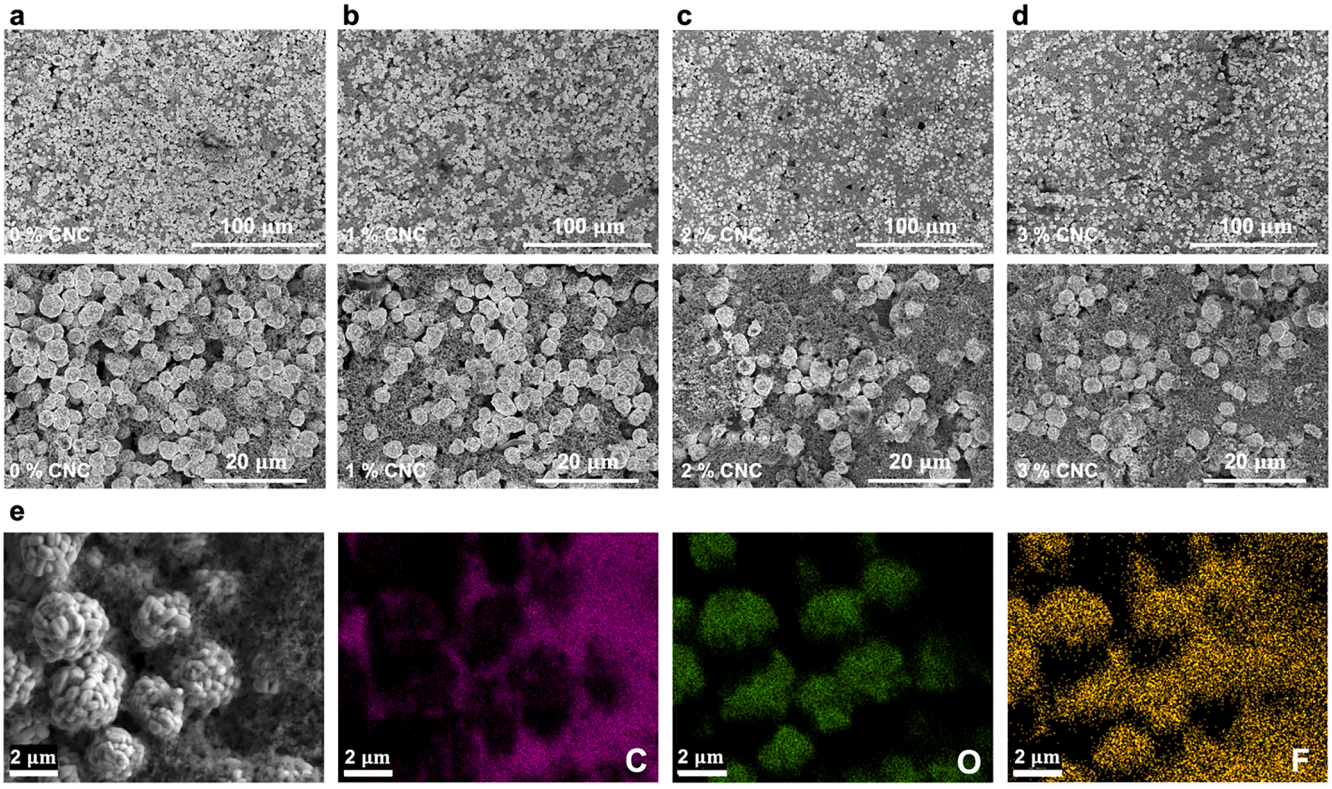

Fig. 3. SEM images of (a) 0 %, (b) 1%, (c) 2%, and (d) 3% CNC electrodes. Elemental mapping of (e) 1% CNC electrode to show the distribution of C, O, and F elements.

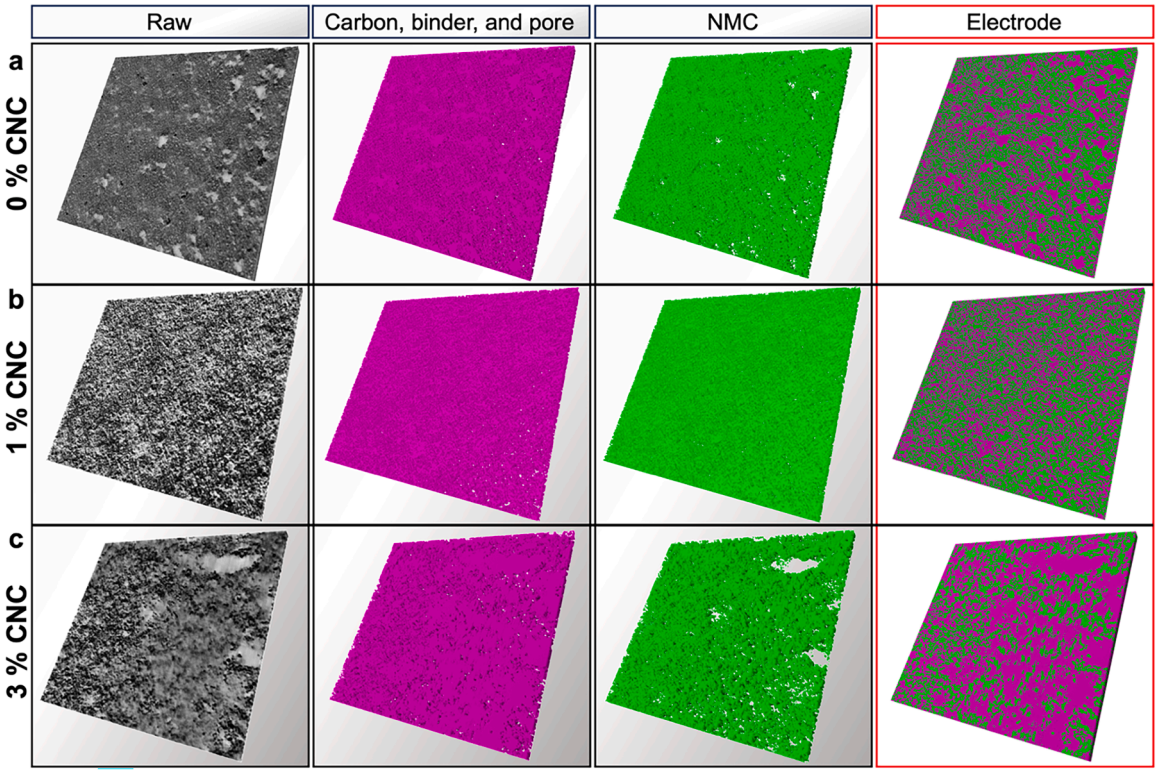

Fig. 4. Reconstructed micro-XCT images of carbon, binder, and pore components (fuchsia), as well as NMC 622 (green) in (a) 0%, (b) 1%, and (c) 3% CNC electrodes.

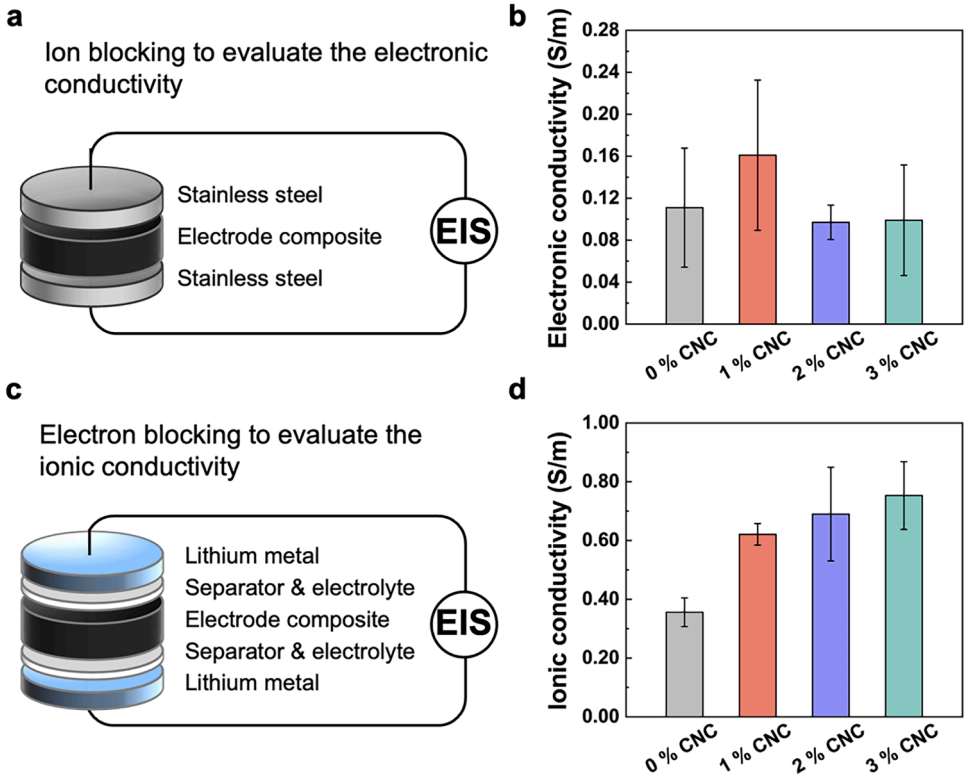

Fig. 5. Effective electronic and ionic conductivities of electrodes with various CNCs contents. (a) Schematics of ion blocking configuration to evaluate the electronic conductivity of electrodes. (b) Electronic conductivity and tortuosity comparison among electrodes. (c) Schematics of the electron blocking setup to evaluate the ionic conductivity of electrodes. (d) Comparison of ionic conductivity of electrodes.

component distribution, a comparative analysis was conducted on three types of electrodes: optimized (with 1% CNCs, Fig. 4a), control (with 0% CNCs, Fig. 4b), and worst (with 3% CNCs, Fig. 4c), building upon prior findings. Compared to the other two electrodes, the 1% CNC electrode exhibits a more uniform component dispersion from the raw data, in which the dark area responds to NMC particles. The utilization of the additional segmentary process was implemented to effectively emphasize the distribution of NMC and other components. Due to unavoidable technology limitations, it is almost impossible to accurately distinguish between carbon, binder, and pore. Consequently, these three components are amalgamated and labeled fuchsia, while NMC particles are colored green. The experimental results reveal that the electrode containing 1% CNCs demonstrates superior uniformity in the distribution of fuchsia and green colors out of the three electrodes, suggesting that the components within the 1% CNC electrode are properly dispersed. In contrast, the incorporation of electrodes consisting of 0 and 3% CNCs resulted in the formation of particle aggregations. Some aggregations are observed on the 0% electrode, while the heavier aggregations are detected in the 3% CNC electrode. Moreover, the 3% CNC electrode is covered with large pieces of fuchsia since the carbon was surfacing on the electrode, agreeing with the SEM results and further demonstrating insufficient dispersion of carbon in this electrode. Consequently, with a solid content of 45%, the introduction of 1% CNCs effectively enhances the carbon distribution throughout the whole electrode, whereas the excessive introduction is counterproductive.

For the purpose of intuitively analyzing the role of CNCs additive in electron and ion transfer kinetics of electrodes, their effective electronic and ionic conductivities were measured and evaluated in coin cells. As shown in Fig. 5a, an ion blocking configuration was applied to evaluate the electronic conductivity using electrochemical impedance spectroscopy (EIS). Fig. 5b summarizes that the electronic conductivity of electrodes with 0, 1, 2, and 3% CNCs are 0.11, 0.16, 0.10, and 0.10 S/m, respectively. Consistent with previous findings, the 1% CNC electrode possesses the highest electronic conductivity among these electrodes

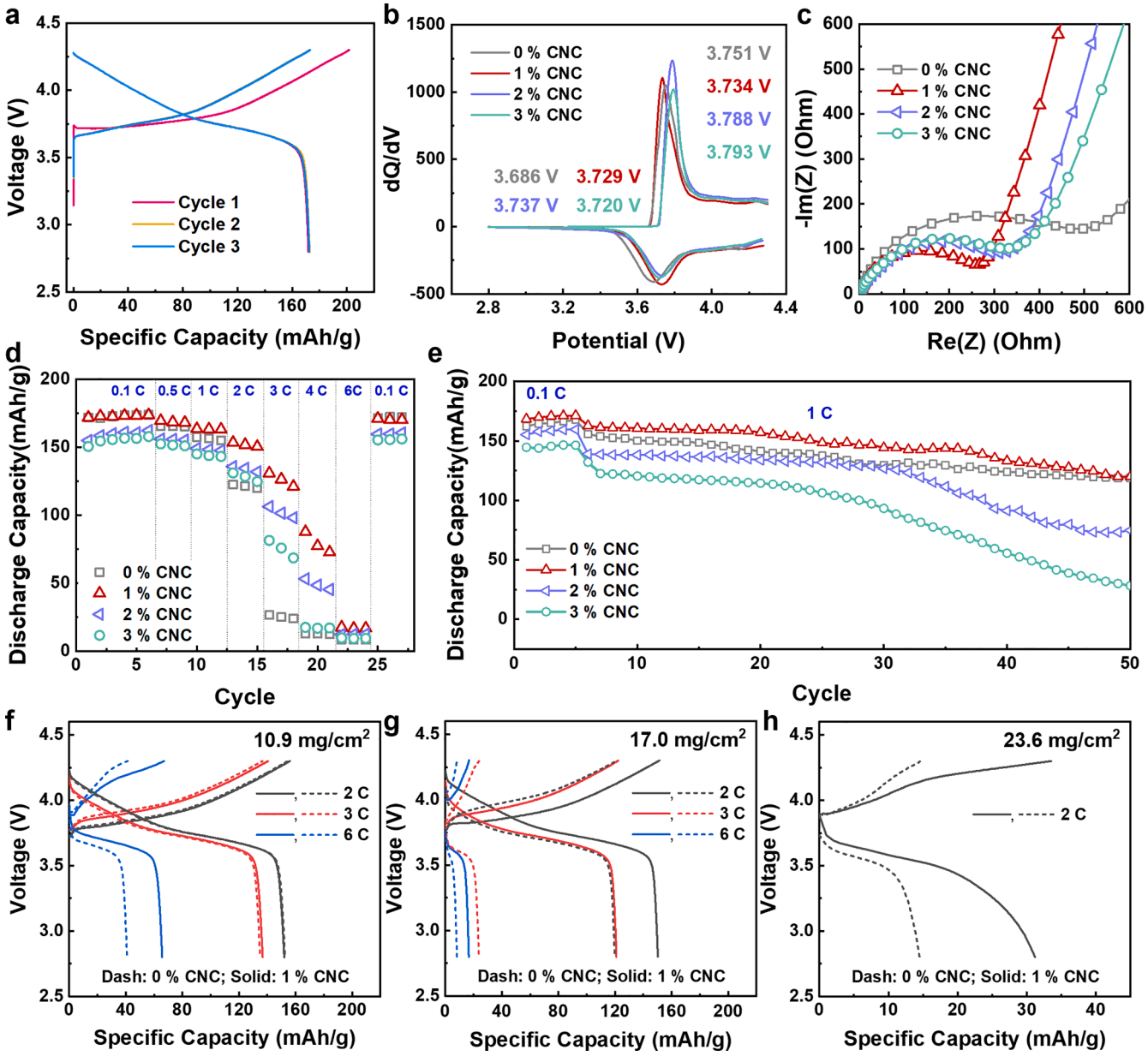

Fig. 6. Electrochemical performances of electrodes. (a) Galvanostatic charge and discharge curves of the initial three curves of 1% CNC electrode at 0.1 C. (b) dQ/dV curves, (c) Nyquist plots, (d) rate performance, and (e) cycling stability of 0, 1, 2, and 3% CNC electrodes. The mass loading of these electrodes is 17.0 mg/cm^2. Galvanostatic charge and discharge curves of 0% and 1% CNC electrodes with mass loadings of (f) 10.9, (g) 17.0, and (h) 23.6 mg/cm^2 at different current rates.

because of the best carbon dispersion. In addition, the ionic conductivity of these electrolyte-filled electrodes was measured using an electron blocking apparatus (Fig. 5c). As portrayed in Fig. 5d, the ionic conductivities of electrolyte-immersed electrodes are 0.36, 0.62, 0.69, and 0.75 S/m for 0, 1, 2, and 3% CNC electrodes, respectively. There is a strong positive association between the added quantity of CNCs and ionic conductivity, demonstrating the advantages of CNC for the electrochemical kinetic of electrode-electrolyte interface. Based on measured conductivity, the corresponding electronic and ionic tortuosity were calculated and compared following our previous work [41]. These results are presented and discussed in **Tables S2–5** and supporting information. Although the accuracy of the tortuosity values remains to be verified due to the lack of model refinement, the trends reasonably demonstrate that 1) the enhanced dispersion of carbon reduces the electronic tortuosity of electrodes, and 2) the CNCs bridge that has been constructed allows effective passage of Li^+ and concurrently reduces the ionic tortuosity of electrodes. As mentioned previously, enhancing effective ionic and electronic conductivities with reducing related tortuosity assists electrodes in accelerating the charge transfer kinetics for fast charging.

The enhanced charge transfer kinetics can be visualized in the improved electrochemical performance of electrodes. Fig. 6a displays the initial three charge and discharge curves of the 1% CNC electrode. There is no abnormal plateau appearing, demonstrating that CNCs are electrochemically stable from 2.8 to 4.3 V. Meanwhile, the first charge and discharge capacities of the 1% CNC electrode are 202 and 172 mAh/g, respectively. The formulation of a cathode electrolyte interface produces an initial coulombic efficiency (ICE) of 85%. **Fig. S6** portrays the charging-discharging curves of 0, 2, and 3% CNC electrodes, presenting ICE of 81, 78, and 77%, respectively. The tendency of electrodes ICE is consistent with their electric conductivity. Fig. 6b portrays the dQ/dV profiles of the 0, 1, 2, and 3% CNC electrodes. A pair of oxidation and redox peaks associated with phase transformations of NMC 622 is observed at around 3.700 V [42]. Additionally, the peak separation indicates a potential gap. The potential gap between anodic and cathodic peaks of the 1% CNC electrode (5 mV) is significantly lower than that of 0% (65 mV), 2% (51 mV), and 3% (73 mV) CNC electrodes, indicating that the 1% CNC electrode possessed superior reaction kinetics and a fainter polarization than the other electrodes. The Nyquist plots of these electrodes are compared in Fig. 6c, and the related fit results and more details are shown in **Fig. S7**. All plots exhibit semicircles in the high-frequency region and Warburg tails in the low-frequency region, which imply the charge transfer resistance and ion diffusion resistance, respectively. Following the fitting results (**Table S1**), the bulk resistance and charge transfer resistance of the 1, 2, 3, and 0% CNC electrodes sequentially increase. All CNCs-included electrodes exhibit much smaller charge transfer resistance than the 0% CNC electrode, suggesting the positive effects of CNC on the charge transfer between the active materials and electrolyte. Furthermore, the diffusion coefficient of electrodes increases with their CNC content elevation, keeping in line with the previous observation. The aforementioned results provide a composite expression of the advantages of CNCs additive for the electrode.

The rate performance of the NMC 622 electrode mixed with various amounts of CNCs additive was evaluated by charging and discharging at different current rates of 0.1, 0.5, 1, 2, 3, 4, and 6 C, in which 1 C equals 180 mAh/g. At 3 C, 1% CNC electrode delivered a sequentially greater discharge capacity of 125 mAh/g than 2% (103 mAh/g), 3% (75 mAh/g), and 0% (15 mAh/g) CNC electrodes. The long-term cycling performance of these electrodes at a charge and discharge rate of 1 C is shown in Fig. 6e, and all cells were initially activated at 0.1 C for five cycles. **Fig. S8** plots the galvanostatic charge and discharge curves of the 1% electrode during cycling at 1C. With increasing cycling numbers, no additional plateaus were observed in all electrodes, suggesting the CNC is electrochemically stable during cycling. However, with the increase of CNC content, the electrode showed a significant increase of overpotential at higher than 35 cycles. The potential causes for the decay might be due to the structure collapse, such as electrode fragmentation and electrode disconnect between the electrode and current collector. The discharge capacity of 0 and 1% CNC electrodes is much more stable than that of 2 and 3% CNC electrodes due to their greater structural stability during charging and discharging. Because of the longer molecule chains, PVDF is a more powerful binder than CNC for connecting the electrode and current collector, capturing all components, and ensuring the structural integrity of electrodes. The bonding capability between 0 and 3% CNC electrodes was evaluated using the tape peeling test (**Fig. S9**). In comparison to the 0% CNC electrode with pure PVDF binder, the 3% CNC electrode with pure CNC binder exhibited a large amount of powder falloff, resulting from the poor bonding among electrode components and between the electrode and current collector. Consequently, optimizing the ratio of CNC to PVDF is essential for electrodes to achieve outstanding capacity at high rates and adequate cycling stability. In this work, 1% CNC addition is helpful in improving the rate performance of electrodes with a negligible impartment for long-term cycle performances.

The capacity advantage between 0 and 1% CNC electrodes is further reflected in the electrode with various mass loadings. **Fig. S10** compares the rate performance of 0 and 1% CNC electrodes at mass loading of 10.9, 17.0, and 23.6 mg/cm^2, and Fig. 6f–h plot the galvanostatic charge and discharge curves of these cells at various current rates. At current rates of 2 and 3 C, no obvious difference is exhibited in electrodes with a mass loading of 10.9 mg/cm^2. In comparison, the overpotential of the two electrodes considerably increased at 6 C, signifying a large capacity of roughly 20 mAh/g. Basically, greater mass loading and higher current rates lead to more noticeable improvements in overpotential gaps decreasing and specific capacity increase. Specifically, a discernible difference appears at 3 C with a mass loading of 17.0 mg/cm^2 and at 2 C with a mass loading of 23.6 mg/cm^2.

The conventional constant current-constant voltage (CC-CV) charging method was employed to showcase the advantages of CNCs on the electrochemical properties of high mass loading electrodes with a thickness of 241 μm. The application of this charging procedure is prevalent in the assessment of electrodes with high mass loading. The Nyquist plots of the electrodes with a high mass loading of 27.0 mg/cm^2 are depicted in Fig. 7a. The bulk resistance differential between the 1% CNC electrode (5.2 Ω) and 0% CNC electrode (22.4 Ω) exhibited a significant increase, in contrast to the preceding electrodes with a low mass loading of 17.0 mg/cm^2, which showed a minor change. Fig. 7b portrays the enhancement of CNCs additive in rate performance. At a high mass loading of 27.0 mg/cm^2, the disparity in capacity between electrodes incorporating 0 and 1% CNC becomes apparent at a low charge rate of 0.5 C. At increased current rates, the electrode containing CNCs additive demonstrates a significant increase in its discharge capacity compared to the traditional additive-free electrodes. Specifically, the 1% CNC electrode exhibits discharge capacities of 128, 87, 50, 30, and 15 mAh/g at current rates of 1, 2, 3, 4, and 6 C, respectively, while the 0% CNC electrode gives discharge capacities of 95, 37, 19, 13, and 9 mAh/g at the corresponding current rates. The analysis of the galvanostatic charge and discharge curves at current rates of 2 and 3 C (Fig. 7c) indicates that the 1% CNC electrode exhibits a lower overpotential and a higher capacity compared to the 0% CNC electrode. Simultaneously, the curves subjected to CC and CC-CV processing suggest that the previous charging method yielded minimal capacity.

Fig. 7d reveals the difference between these two charging methods. First, an augmentation in the high charging current rates leads to an elevation in the ohmic polarization, causing the electrode voltage to swiftly approach the cutoff voltage. Second, the extremely short charging time hinders the comprehensive reaction of electrode materials, particularly due to the need for a greater distance of charge transfer in the case of thick electrodes with high mass loading. After CC charging, the CV process performed next ensures adequate time and prevents incomplete electrochemical reactions. Therefore, the CC-CV

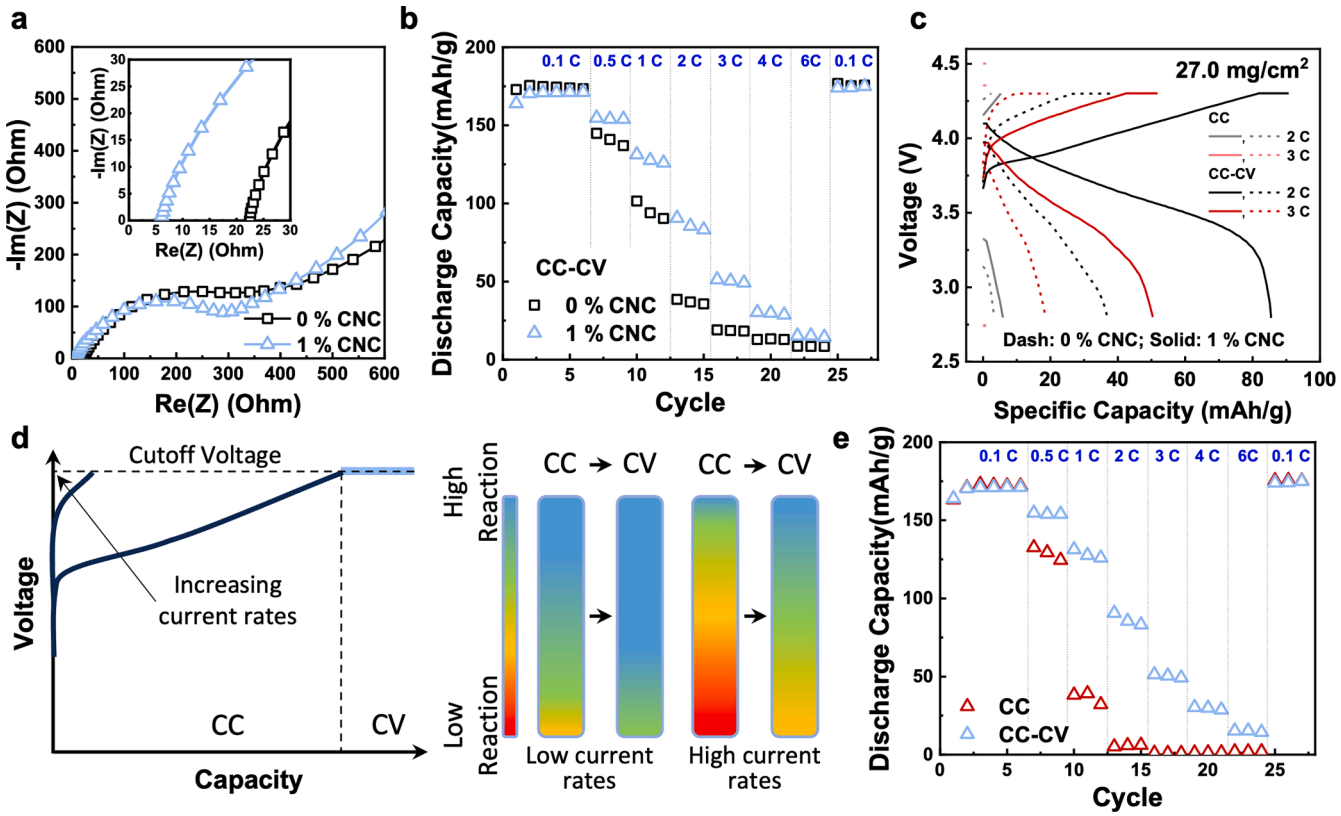

Fig. 7. Electrochemical performances of thick electrodes with a mass loading of 27.0 mg/cm^2. (a) Nyquist plots and (b) rate performance of 0% and 1% CNC electrodes using the CC-CV charge process. (c) Charge and discharge curves of 0% and 1% CNC electrodes using the CC and CC-CV charging process. (d) Schematic of the effect of the charging method on thick electrodes. (e) Rate performance of the 1% CNC electrodes charged with CC and CC-CV process.

method is helpful, especially when it is associated with thick electrodes approaching the cutoff voltage due to high over-polarization. Fig. 7e presents a comparison between 1% CNC electrodes charged through the CC and the CC-CV methods. It is evident that the electrodes acquired by the latter charging technique exhibit a more rational capacity when subjected to high current rates of 1 C and higher. This facilitates showing the advantages after kinetic optimization in thick electrodes. Meanwhile, no loss of capacity occurred when returning to 0.1 C, suggesting that the CC-CV method does not cause damage to the electrodes.

In addition to mass loading, the mixing procedure also affects the rate performance of these electrodes by changing the dispersion of components. **Fig. S11** shows the other two slurry preparation processes, and the rate performance of corresponding electrodes is compared in **Figs. S12** and **S13**. Despite replacing a variety of preparation approaches leading to changes in the discharge capacity of electrodes, it is confirmable that the 1% CNC electrode consistently outperforms the 0% CNC electrode. Simultaneously, the electrodes produced using method A at a charge rate of 6 C illustrate the correlation between the disparity in capacity between electrodes with 0% and 1% CNCs and their mass loading, as depicted in **Fig. S12b**. Although more profound optimization is required to enhance the capacity of electrodes with high mass loading in the future, CNCs are a reliable and effective additive to enhance the fast-charging capacity of thick electrodes.

The experimental results show that CNCs additions increase both electronic conductivity (1% loading only) and ionic conductivity (all loadings). Both effects appear to influence the increased capacity at fast charging rates. To provide additional quantitative insight into these combined effects, simulations using the Newman P2D model in COMSOL Multiphysics© were employed [43]. Specifically, performance from the 0% CNC (Control group) was compared to the 1% CNC electrodes (highest performing in experiments) and 3% (some improvement over 0% CNC). The simulations were based on measured electronic and ionic conductivity values for the 0% CNC electrode (0.11 S/m and 0.36 S/m, respectively), the 1% CNC electrode (0.16 S/m and 0.62 S/m, respectively) and the 3% CNC electrode (0.1 S/m and 0.75 S/m, respectively).

The simulations examined several C-rates and mass loadings corresponding to the experiments to assess the model's accuracy over a wide range of conditions. The results comparing simulated voltage profiles with experiments are shown in **Fig. S14**, and capacity predictions between 0, 1, and 3% CNC groups are compared in **Fig. S15**. Generally, 1% CNC had the most improved capacity compared to 0% CNCs. The calculated results are similar in trend to the experimental data, where improvements are more substantial for thicker electrodes (**Fig. S15**). These trends are consistent with the hypothesis that the improved capacity can be attributed to both improved electronic conductivity and ionic conductivity in the 1% CNC electrode compared to the 0% CNC electrode. Additionally, the 3% CNC group had a higher capacity than the 0% CNC group but a lower capacity than the 1% CNC group. This can be attributed to the 3% CNC electrode having a higher ionic conductivity than the 0% group but lower electronic conductivity than the 1% group. Specifically, improvements in electronic conductivity had a greater impact on performance than improvements in ionic conductivity because the electronic conductivity was lower than the ionic conductivity of all three electrodes.

3. Conclusion

In this study, we proposed the utilization of cost-effective, environmentally friendly, and biodegradable CNCs additive to enhance the capacity of the thick NMC 622 cathode at high current rates. Specifically, this is the first additive to simultaneously enhance electronic and ionic conductivity to accelerate the kinetic of electrodes. CNCs enhance the carbon dispersion throughout whole electrodes and construct an interconnected network for electron transfer; simultaneously, stacked CNCs

establish a Li^+ transport bridge, thereby shortening the length of the ion transfer route. In this work, the NMC 622 electrodes composed with 1% CNCs exhibited the most favorable electrochemical performance. Upon conducting a comparison between the 1% CNC electrode and the 0% CNC electrode, notable enhancements are observed. Specifically, the former delivered greater electronic conductivity (0.16 vs. 0.11 S/m), higher ionic conductivity (0.62 vs. 0.36 S/m when immersed in the liquid electrolyte), improved reaction kinetics (with potential gaps of 5 vs. 65 mV), and consequently demonstrated superior specific capacities at high rates. At a mass loading of 17.0 mg/cm^2, the 1% CNC electrode exhibited a capacity about eight times greater than the electrode lacking CNCs (125 vs. 15 mAh/g) at a current rate of 3 C and nearly seven times greater (72 vs. 10 mAh/g) at a current rate of 4 C. Using the traditional CC-CV charging method for the electrodes with high mass loading of 27.0 mg/cm^2, the 1% CNC electrode delivers capacity of 128 mAh/g at 1 C, which is much higher than that of 0% CNC electrode with capacity of 95 mAh/g. Additionally, the 1% CNC electrode exhibits capacities of 128, 87, 50, 30, and 15 mAh/g at current rates of 1, 2, 3, 4, and 6 C, respectively. The capacities of this electrode increase twofold compared to the electrode without CNCs additive at the corresponding current rates. Highly repeatable experiments and investigations have demonstrated that the incorporation of CNCs in the thick electrodes leads to enhanced fast-charging capacity. The aforementioned trends and conclusions were simultaneously validated and reproduced by both theoretical simulation and experimental findings. Overall, the adoption of a limited amount of readily available CNCs additive is a rational low-cost strategy for improving the fast charging capability of electrodes, and this approach is very practical for immediate industrialized and commercialized applications.

4. Experimental section

4.1. Materials

Microcrystalline cellulose and 98% sulfuric acid were supplied by Sigma-Aldrich (United States). Kureha 7200 PVDF was purchased from the Kureha firm in Japan. The polycrystalline $LiNi_{0.6}Mn_{0.2}Co_{0.2}O_2$ (NMC 622) was supplied by Easpring Material Technology Co., LTD. in China. The Super P and aluminum foil current collector were supplied by MTI Co., USA. Fisher Science Education in the United States provided NMP. Prior to ink production, NMC 622 and Super P powders were dried in a vacuum oven (MTI Co., USA) for at least 12 h at 100°C. No special treatment was given to any of the materials.

4.2. CNC synthesis

Our previous work laid the groundwork for the CNC acid hydrolysis process [44]. 30 g microcrystalline cellulose was mechanically stirred continuously for 40 min at 45°C with 300 mL 64 wt.% sulfuric acid. To halt the process, ten times the volume of water was used. The suspensions were cleaned by centrifuging at 4000 rpm with deionized water. The centrifuge step was completed after the supernatant became turbid. To remove the remaining acid, the suspensions were dialyzed with deionized water via dialysis membranes (molecular weight cutoff of 12, 000- 14,000) until the water pH was about 7. FreeZone 6 (Labconco Co., USA) was used to freeze-dry the CNC suspension.

4.3. Electrode preparation

PVDF particles were dissolved in NMP at a 10% concentration before usage, and freeze-dried CNC flacks were dispersed in NMP at a 1% concentration. Following computation, a certain amount of PVDF and CNC was diluted and mixed to produce 2.5 weight percent binders. The active component and conductive additive were then combined with a binder in the following weight ratio: NMC 622: Super P: binder = 92: 5: 3 homogeneous slurries with 45% solid content were generated. The slurries were then deposited using a doctor blade onto an aluminum sheet and dried overnight in a vacuum oven at 100°C. All mass loadings mentioned in this manuscript are the mass loading of active materials.

4.4. Characterization methods

CNC morphology was studied using an atomic force microscope (Bruker Dimension Icon-Raman AFM). CNC structure and orientation were described using X-ray diffraction (X'Pert Pro, Philips). The Fourier transform infrared (FTIR) (Cary 630 FTIR, Agilent) was utilized to analyze the functional groups of synthesized CNC. The rheological characteristics of electrode slurries were measured using a hybrid rheometer (TA Instruments Discovery HR-30) with a flat Peltier plate. On a Hitachi S4800 at 3 kV, the electrodes were examined using scanning electron microscopy and energy-dispersive X-ray spectroscopy. In accordance with ASTM D3330, Method A, tape peeling was performed using 3M 6122 MP Scotch Magic Tape.

4.5. X-ray computed tomography (XCT)

The XCT measurements were performed using a Zeiss Xradia Versa 520 XCT unit with a 60 kV X-ray energy at 5W. A 20× scintillator objective was used to maximize the resolution with a 2 × 2 binning, resulting in a voxel size of 0.69 μm. The data were obtained over a sample rotation of $\omega = 360^\circ$ with 1601 intervals at equal steps. A Dragonfly PRO v.3.5 software was used for the data processing and analyses.

4.6. Electrochemistry characterization

In all electrochemical measurements, the electrolyte was 1.2 M LiPF6 dissolved in EC: EMC= 3: 7 by weight (Gen 2). A total of 80 μL of electrolyte was added to the cell construction. The separator Celgard 2400 (thickness in 25 μm) was utilized. At room temperature, electrochemical impedance spectroscopy was done with a Biologic SP150 electrochemical station in the frequency range of 1 MHz to 100 mHz. Electrode electronic and ionic conductivities were estimated using the equation =l/AR, where (S/m) is conductivity, A (m^2) is an area, and R (Ω) is resistance. Before the calculation, the resistances of other parts except the electrodes were measured and subtracted. The rate performance and cycle stability of electrodes were evaluated using a LANDT 8-channel tester (Wuhan LAND Electronic Co., Ltd.). The rate performance of electrodes with mass loading of 10.9, 17.0, and 23.6 mg/cm^2 were charged and discharged at various C-rates, first at 0.1 C for six cycles, then at 1 C, 2 C, 4 C, and 6 C for three cycles, and lastly back to 0.1 C for three cycles. For the thick electrode with 27.0 mg/cm^2, electrodes were charged with CC-CV method at C/3 and discharged at various rates. 1 C equals 180 mAh/g. At room temperature, all electrochemical experiments were carried out.

4.7. Modeling method

Simulations using the Newman P2D model in COMSOL Multiphysics© were used to determine how the proposed change in electronic conductivity alters the capacity during fast charging. The governing equations for this model are summarized elsewhere [45], and a summary of the parameters used in this model is given in SI. The cathode, electrolyte, and separator properties are defined in **Tables S6–S8**, except for concentration-dependent parameters, which are shown in **Fig. S16**, and the equilibrium potential, which is shown in **Fig. S17**. Functional relationships between various constants and concentration-dependent properties (e.g., the reaction rate constant and the exchange current density) are also specifically defined in our previous work [46].

Since the most improvement and most differences in conductivity and high C-rate capacity were observed between the 0% CNC (Control

group) and 1% CNC group, only these groups' conditions were considered. In the simulations, the 1% CNC group had increased effective electronic conductivity compared to the 0% CNC control group (0.11 S/m vs. 0.16 S/m); the 1% CNC also had higher ionic conductivity compared to the 0% CNC control (0.36 S/m and 0.62 S/m respectively at 1200mol/m^3 $LiPF_6$ concentration).

CRediT authorship contribution statement

Ying Wang: Writing – review & editing, Writing – original draft, Visualization, Validation, Project administration, Methodology, Investigation, Formal analysis, Data curation, Conceptualization. **Aleksandar S. Mijailovic:** Writing – review & editing, Writing – original draft, Validation, Software, Investigation. **Tongtai Ji:** Software. **Ercan Cakmak:** Resources, Investigation. **Xianhui Zhao:** Resources. **Luyao Huang:** Methodology, Investigation. **Brian W. Sheldon:** Writing – review & editing, Supervision, Investigation. **Hongli Zhu:** Writing – review & editing, Writing – original draft, Validation, Supervision, Resources, Project administration, Methodology, Investigation, Funding acquisition, Formal analysis, Data curation, Conceptualization.

Declaration of competing interest

The authors declare that they have no known competing financial interests or personal relationships that could have appeared to influence the work reported in this paper.

Data availability

The data that has been used is confidential.

Acknowledgment

This research is supported by the U.S. Department of Energy's Office of Energy Efficiency and Renewable Energy (EERE), through the Advanced Manufacturing Office under grant number DE-EE0009111. The authors appreciate Dr. Sanjeev Mukerjee and Dr. Huidong Dai from Northeastern University for the use of atomic force microscopy. This manuscript has been authored by UT-Battelle, LLC, under contract DE-AC05-00OR22725 with the US Department of Energy (DOE). The US government retains and the publisher, by accepting the article for publication, acknowledges that the US government retains a nonexclusive, paid-up, irrevocable, worldwide license to publish or reproduce the published form of this manuscript, or allow others to do so for US government purposes. DOE will provide public access to these results of federally sponsored research in accordance with the DOE Public Access Plan (http://energy.gov/downloads/doe-public-access-plan).

Supplementary materials

Supplementary material associated with this article can be found, in the online version, at doi:10.1016/j.ensm.2024.103546.

References

[1] C.Y. Wang, et al., Fast charging of energy-dense lithium-ion batteries, Nature 611 (7936) (2022) 485–490.
[2] J.W. Choi, D. Aurbach, Promise and reality of post-lithium-ion batteries with high energy densities, Nat. Rev. Mater. 1 (4) (2016) 1–16.
[3] S. Zhao, et al., Towards high-energy-density lithium-ion batteries: strategies for developing high-capacity lithium-rich cathode materials, Energy Storage Mater. 34 (2021) 716–734.
[4] D. Cao, et al., Processing strategies to improve cell-level energy density of metal sulfide electrolyte-based all-solid-state Li metal batteries and beyond, ACS Energy Lett. 5 (11) (2020) 3468–3489.
[5] Y. Kuang, et al., Thick electrode batteries: principles, opportunities, and challenges, Adv. Energy Mater. 9 (33) (2019) 1901457.
[6] Z. Du, et al., Understanding limiting factors in thick electrode performance as applied to high energy density Li-ion batteries, J. Appl. Electrochem. 47 (2017) 405–415.
[7] T.H. Le, Y. Kim, H. Yoon, Electrical and electrochemical properties of conducting polymers, Polymers 9 (4) (2017) 150.
[8] F. Zou, A. Manthiram, A review of the design of advanced binders for high-performance batteries, Adv. Energy Mater. 10 (45) (2020) 2002508.
[9] H. Chen, et al., Exploring chemical, mechanical, and electrical functionalities of binders for advanced energy-storage devices, Chem. Rev. 118 (18) (2018) 8936–8982.
[10] Y. Zhao, et al., Versatile zero-to three-dimensional carbon for electrochemical energy storage, Carbon Energy 3 (6) (2021) 895–915.
[11] C.D. Quilty, et al., Electron and ion transport in lithium and lithium-ion battery negative and positive composite electrodes, Chem. Rev. 123 (4) (2023) 1327–1363.
[12] H. Ren, et al., Enhancing composite electrode performance: insights into interfacial interactions, Chem. Commun. (2024).
[13] C. Meyer, et al., Characterization of the calendering process for compaction of electrodes for lithium-ion batteries, J. Mater. Process. Technol. 249 (2017) 172–178.
[14] W. Porcher, et al., Optimizing the surfactant for the aqueous processing of LiFePO4 composite electrodes, J. Power Sources 195 (9) (2010) 2835–2843.
[15] Y. Wang, et al., Opening twisted polymer chains for simultaneously high printability and battery fast-charge, Energy Storage Mater. 55 (2023) 42–54.
[16] D. Liu, et al., An effective mixing for lithium ion battery slurries, Adv. Chem. Eng. Sci. 4 (04) (2014) 515.
[17] J.K. Mayer, et al., Influence of the carbon black dispersing process on the microstructure and performance of Li-ion battery cathodes, Energy Technol. 8 (2) (2020) 1900161.
[18] J. Haverkort, A theoretical analysis of the optimal electrode thickness and porosity, Electrochim. Acta 295 (2019) 846–860.
[19] M. Ebner, et al., Tortuosity anisotropy in lithium-ion battery electrodes, Adv. Energy Mater. 4 (5) (2014) 1301278.
[20] Y. Wang, et al., Designing low tortuosity electrodes through pattern optimization for fast-charging, Small Methods 7 (4) (2023) 2201344.
[21] H. Ren, et al., Manufacturing water-based low-tortuosity electrodes for fast-charge through pattern integrated stamping, Energy Environ. Mater. (2023) e12584.
[22] I. Capron, O.J. Rojas, R. Bordes, Behavior of nanocelluloses at interfaces, Curr. Opin. Colloid Interface Sci. 29 (2017) 83–95.
[23] Y. Li, et al., Nanocellulose as green dispersant for two-dimensional energy materials, Nano Energy 13 (2015) 346–354.
[24] H. Zhang, et al., Using cellulose nanocrystal as adjuvant to improve the dispersion ability of multilayer graphene in aqueous suspension, Front. Bioeng. Biotechnol. 9 (2021) 638744.
[25] C. Yang, et al., Copper-coordinated cellulose ion conductors for solid-state batteries, Nature 598 (7882) (2021) 590–596.
[26] Z. Wang, et al., Dynamic networks of cellulose nanofibrils enable highly conductive and strong polymer gel electrolytes for lithium-ion batteries, Adv. Funct. Mater. (2023) 2212806.
[27] S. Jing, et al., The critical roles of water in the processing, structure, and properties of nanocellulose, ACS Nano 17 (22) (2023) 22196–22226.
[28] H. Yang, N. Wu, Ionic conductivity and ion transport mechanisms of solid-state lithium-ion battery electrolytes: a review, Energy Sci. Eng. 10 (5) (2022) 1643–1671.
[29] Y. Ye, et al., Cellulose-based ionic conductor: an emerging material toward sustainable devices, Chem. Rev. 123 (15) (2023) 9204–9264.
[30] Y. Lu, et al., Sulfonic groups originated dual-functional interlayer for high performance lithium–sulfur battery, ACS Appl. Mater. Interfaces 9 (17) (2017) 14878–14888.
[31] X. Wang, et al., Hydroxyl on the filler surface promotes Li+ conduction in PEO all-solid-state electrolyte, Solid State Ion. 372 (2021) 115768.
[32] A. Mukhopadhyay, et al., Stable and highly ion-selective membrane made from cellulose nanocrystals for aqueous redox flow batteries, Nano Lett. 19 (12) (2019) 8979–8989.
[33] H. Zhu, et al., Tin anode for sodium-ion batteries using natural wood fiber as a mechanical buffer and electrolyte reservoir, Nano Lett. 13 (7) (2013) 3093–3100.
[34] H. Zhu, et al., A gravure printed antenna on shape-stable transparent nanopaper, Nanoscale 6 (15) (2014) 9110–9115.
[35] Y. Habibi, L.A. Lucia, O.J. Rojas, Cellulose nanocrystals: chemistry, self-assembly, and applications, Chem. Rev. 110 (6) (2010) 3479–3500.
[36] Y. Tang, et al., Preparation and characterization of nanocrystalline cellulose via low-intensity ultrasonic-assisted sulfuric acid hydrolysis, Cellulose 21 (2014) 335–346.
[37] N.A.H. Shazali, et al., Characterization and cellular internalization of spherical cellulose nanocrystals (CNC) into normal and cancerous fibroblasts, Materials 12 (19) (2019) 3251.
[38] T. Zhang, et al., Aminosilane-grafted spherical cellulose nanocrystal aerogel with high CO2 adsorption capacity, Environ. Sci. Pollut. Res. 26 (16) (2019) 16716–16726.
[39] F. Pignon, et al., Breakdown and buildup mechanisms of cellulose nanocrystal suspensions under shear and upon relaxation probed by SAXS and SALS, Carbohydr. Polym. 260 (2021) 117751.
[40] D. Cao, et al., Amphipathic binder integrating ultrathin and highly ion-conductive sulfide membrane for cell-level high-energy-density all-solid-state batteries, Adv. Mater. 33 (52) (2021) 2105505.

[41] A.M. Stavola, et al., Lithiation gradients and tortuosity factors in thick NMC111-argyrodite solid-state cathodes, ACS Energy Lett. 8 (2) (2023) 1273–1280.
[42] J. Choi, et al., Relationship of chemical composition and moisture sensitivity in LiNixMnyCo1− X− YO2 for lithium-ion batteries, J. Electrochem. Energy Convers. Storage 18 (4) (2021).
[43] S. Shi, et al., Multi-scale computation methods: their applications in lithium-ion battery research and development, Chin. Phys. B 25 (1) (2015) 018212.
[44] Z. Cheng, et al., Tuning chiral nematic pitch of bioresourced photonic films via coupling organic acid hydrolysis, Adv. Mater. Interfaces 6 (7) (2019) 1802010.
[45] A.S. Mijailovic, et al., Analytical and numerical analysis of lithium plating onset in single and bilayer graphite electrodes during fast charging, J. Electrochem. Soc. 169 (6) (2022) 060529.
[46] A.S. Mijailovic, et al., A" Master Curve" describing reaction inhomogeneity and plating onset during fast-charging of graphite electrodes, J. Electrochem. Soc. (2023).